Imaging the inside of a Continuous Nanoceramic Synthesizer under Supercritical Water Conditions Using High-Energy Synchrotron X-Radiation

Vesna Middelkoop,[†,‡] Paul Boldrin,[§] Matthew Peel,[||] Thomas Buslaps,[||] Paul Barnes,*[,†,‡] Jawwad A. Darr,[§] and Simon D. M. Jacques[†,‡]

Industrial Materials Group, Department of Chemistry, University College London, 20 Gordon Street, London WC1H 0AJ, United Kingdom, School of Crystallography, Birkbeck College, Malet Street, London WC1E 7HX, United Kingdom, The Clean Materials Technology Group, Department of Chemistry, University College London, 20 Gordon Street, London WC1H 0AJ, United Kingdom, and European Synchrotron Radiation Facility, 38043 Grenoble, France

Received January 14, 2009. Revised Manuscript Received April 20, 2009

Continuous hydrothermal flow synthesis (CHFS) offers a controllable route to the production of nanocrystalline materials. We describe the application of tomographic X-ray methods to image, for the first time, crystallization at the interior of an in operando CHFS reactor. In the experiment, the steady-state formation of nanoparticulate CeO_2 was followed: the synthesis proceeds by rapid hydrolysis of cerium ammonium nitrate and hydrothermal coprecipitation in a near/super-critical water environment ($T = 340-450$ °C, $P = 24$ MPa). The results identify the location of particle growth with accompanying indications of crystallite size, and also reveal the build-up of material on the reactor wall during long syntheses. The imaging represents a significant achievement in that information of this kind can be gleaned from such an inhospitable environment as that of a CHFS reactor. The novel combination of tomographic angle- and energy-dispersive diffraction employed was particularly appropriate for this in situ study, where the CHFS apparatus could not be rotated (as is required in conventional tomography methods). This imaging capability offers new insights into the synthesis process, which can lead to optimization, better reactor design, and adaptation toward industrial application.

Introduction

Supercritical water is essentially a single (fluid) phase of water at or above its critical point ($T_c = 374$ °C, $P_c = 22.1$ MPa). Under such conditions, the properties of water are very different from water at standard temperature and pressure; supercritical water acts as an ideal reaction medium for rapid hydrolysis and for high nucleation rates and crystallization of ceramic oxides from salts. It has been known since the early 1990s[1−4] that supercritical water (hydrothermal) crystallization methods can be converted from a batch to a continuous production processes, particularly for producing fine metal oxide nanoparticles, e.g., Fe_2O_3, Fe_3O_4, Co_3O_4, NiO, TiO_2, ZrO_2, $Ce_xZr_{1-x}O_2$, as well as hydroxyapatite, $NiCo_2O_4$ spinels, and CeO_2.[5−15] In the CHFS process, a stream of superheated water is mixed with a counter-current flow of metal salt (or several salts) solution that can be in the presence of other redox agents, resulting in rapid and continuous synthesis of nanosized oxides or hydroxide particles. The nanoparticles are then cooled and collected at the exit of the apparatus as an aqueous slurry (after depressurization). Despite the promise of CHFS methods, it has been difficult to gather direct information on the actual CHFS process on account of the required construction of stainless steel reactors and the inhospitable environment within. Previous studies have sought to understand mixing zone dynamics using computational modeling,[15,17]

* Corresponding author. E-mail: p.barnes@mail.cryst.bbk.ac.uk.
[†] Industrial Materials Group, University College London.
[‡] Birkbeck College.
[§] The Clean Materials Technology Group, University College London.
[||] European Synchrotron Radiation Facility.

(1) Arai, K.; Ajiri, T. Patent 5 635 154, 1997; http://www.freepatentsonline.com/5635154.html.
(2) Adschiri, T.; Kanazawa, K.; Arai, K. *J. Am. Ceram. Soc.* **1992**, *75*, 1019.
(3) Cansell, F.; Chevalier, B.; Demourgues, A.; Etourneau, J.; Even, C.; Garrabos, Y.; Pessey, V.; Petit, S.; Tressaud, A.; Weill, F. *J. Mater. Chem.* **1999**, *9*, 67.
(4) Galkin, A. A.; Kostyuk, B. G.; Lunnin, V. V.; Poliakoff, M. *Angew. Chem.* **2000**, *39*, 2738.
(5) Adschiri, T.; Hakuta, Y.; Arai, K. *Ind. Eng. Chem. Res.* **2000**, *39*, 4901.
(6) Adschiri, T.; Hakuta, Y.; Sue, K.; Arai, K. *J. Nanopart. Res.* **2001**, *3*, 227.
(7) Hakuta, Y.; Ura, H.; Hayashi, H.; Arai, K. *Mater. Chem. Phys.* **2005**, *93*, 466.
(8) Darr, J. A.; Poliakoff, M. *Chem. Rev.* **1999**, *99*, 495.
(9) Boldrin, P.; Hebb, A. K.; Chaudhry, A. A.; Otley, L.; Thiebaut, B.; Bishop, P.; Darr, J. A. *Ind. Eng. Chem. Res.* **2007**, *46*, 4830.
(10) Weng, X.; Boldrin, P.; Abrahams, I.; Skinner, S. J.; Darr, J. A. *Chem. Mater.* **2007**, *19*, 4382.
(11) Boldrin, P.; Chaudhry, A. A.; Khalid, F.; Darrm, J. A.; Rehman, I. U. *J. Chem. Soc., Chem. Commun.* **2006**, 2286.
(12) Cabañas, A.; Darr, J. A.; Lester, E.; Poliakoff, M. *Chem. Commun.* **2000**, 901.
(13) Cabañas, A.; Darr, J. A.; Lester, E.; Poliakoff, M. *J. Mater. Chem.* **2001**, *11*, 561.
(14) Lester, E. H.; Azzopardi, B. J. Patent WO/2005/077505, 2005; http://www.wipo.int/pctdb/en/wo.jsp?IA=GB2005000483&DISPLAY=DESC.
(15) Lester, E.; Blood, P.; Denyer, J.; Giddings, D.; Azzopardi, B.; Poliakoff, M. *J. Supercrit. Fluids* **2006**, *37*, 209.
(16) Blood, P.; Denyer, J.; Azzopardi, B. J.; Poliakoff, M.; Lester, E. *Chem. Eng. Sci.* **2004**, *59*, 2853.

10.1021/cm900118z CCC: $40.75
Published on Web 05/11/2009

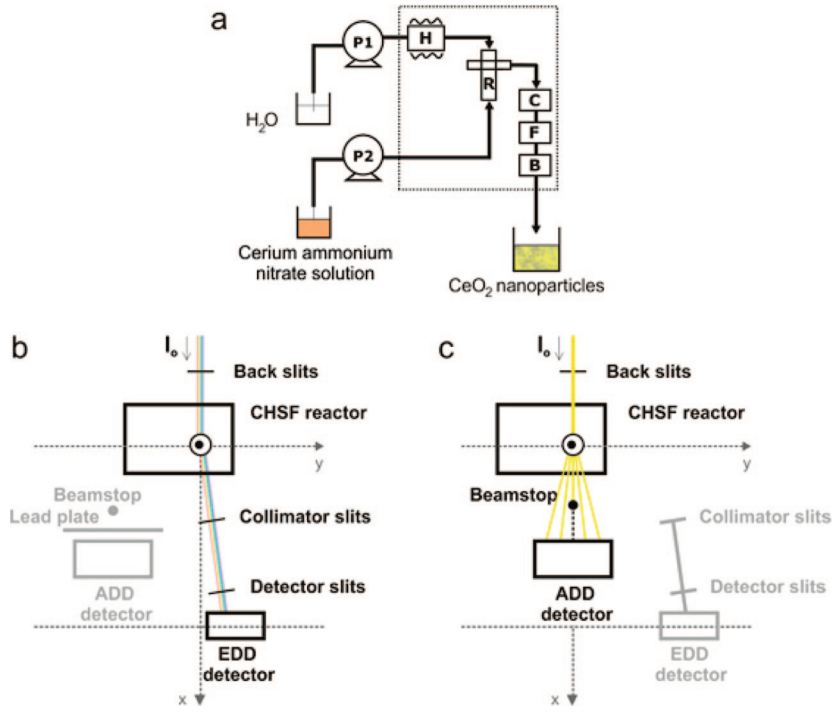

Figure 1. Schematic diagrams of the experimental setup for a combined TEDDI/TADDI tomographic in situ study of continuous crystallization of CeO_2 nanoparticles under supercritical conditions on ESRF station ID15A. (a) Flow diagram of the portable supercritical water continuous hydrothermal flow synthesis (CHFS) system, consisting of two pumps (P1 and P2) delivering both reactants at 25 mL min^{-1} to a counter-current mixing zone (R) (H = (pre)heater, C = cooler, F = filter, B = back-pressure regulator for maintaining upstream pressure; 316 stainless steel Swagelok tubing and high-pressure fittings are used throughout with various pressure/temperature gauges). (b) The reactor in energy-dispersive mode (TEDDI). (c) The reactor in angle-dispersive mode (TADDI). The apparatus can be switched between modes within seconds by moving the *xyz* stage with the reactor about 50 mm along *y*; the detectors are also separately repositioned.

or physical modeling using simulated[15,16] or actual[18] supercritical fluids to visualize the flow using dyes; such studies illustrate ideal mixing scenarios that in turn further highlight the need for a direct in situ probe. X-ray scattering/diffraction has the required attributes to be such a probe and indeed it has been successfully used, in both small- and wide-angle scattering modes, by Bremholm et al.[19] to follow the formation of Fe_3O_4 nanoparticles at 350 °C/40 MPa and below. The latest multimodal (diffraction, fluorescence and absorption) tomographic method of Bleuet et al.[20] demonstrates sensitivity in phase mapping of unidentified nanocrystalline materials, but its scanning operation, involving series of both linear and rotation steps, is not suitable for complex hydroengineering systems such as the CHFS reactor.

Results and Discussion

In this study, we have used a new highly sensitive and nondestructive imaging combination, TÆDDI (Tomography angle and energy-dispersive diffraction imaging) to construct spatial maps of the supercritical water crystallization environment inside the mixing zone during actual operation of a complex CHFS reactor. In so doing, we have also extended the modality of diffraction tomography so that it utilizes both energy- and angle-dispersive diffraction data, thereby gaining two complementary data sets on the crystallization process. This is the first in situ imaging study of nanoparticle synthesis in a continuous hydrothermal flow synthesizer mixing zone, using both monochromatic and polychromatic X-rays. The results yield remarkable images of nanoparticle crystallization in the mixing zone and provide the clearest view so far of the synthesis process. Such information will be invaluable for both modeling studies and future reactor designs with improved mixing arrangements.

A schematic of the CHFS reactor is given in Figure 1a. The basic operation consists of the delivery of two aqueous reactants (via two flow tubes) to a mixing zone (counter-current mixer) [9−11] where the nanoparticle products are formed and then flow out to be extracted in continuous fashion. The complexities arise from one of the continuously fed reactants being supercritical water delivered via a narrow tube contained inside another (outer) tube which delivers the second reactant, a metal salt solution (i.e., a counter-current mixing arrangement). The actual mixing point is a region at or close to the terminus of the inner-tube of the counter-current mixer where nanoparticles are expected to be formed; Figure 3a (see later) reveals the actual size, location, and nature of the mixing region, this being a principal objective of the tomographic study. For this purpose, a well-defined synthesis was chosen: the production of nanosized ceria [CeO_2] from continuous mixing of 0.25 M cerium ammonium nitrate [$Ce(NH_4)_2(NO_3)_6$] aqueous solution at room temperature

(17) Wakashima, Y.; Suzuki, A.; Kawasaki, S.; Matsui, K.; Hakuta, Y. *J. Chem. Eng. Jpn.* **2007**, *40*, 622.
(18) Aizawa, T.; Masuda, Y.; Minami, K.; Kanakubo, M.; Nanjo, H.; Smith, R. L. *J. Supercrit. Fluids* **2007**, *43*, 222.
(19) Bremholm, M.; Jensen, H.; Brummerstedt Iversen, S.; Brummerstedt Iversen, B. *J. Supercrit. Fluids* **2007**, *44*, 385.
(20) Bleuet, P.; Welcomme, E.; Dooryée, E.; Susini, J.; Hodeau, J.-L.; Walter, P. *Nat. Mater.* **2008**, *7*, 468.

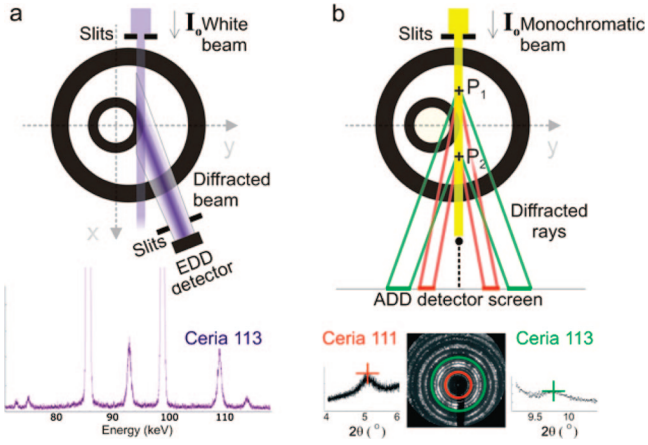

Figure 2. Schematic diagrams (not to scale) illustrating the principles of (a) TEDDI, showing diffraction from a discrete volume, defined by the incident and diffracted beam slits, which is detected by an energy-discriminating device; a well-resolved energy-dispersive diffraction pattern is shown beneath with the position of, for example, the ceria 113 reflection indicated. (b) TADDI, showing angle-dispersed diffraction from different reflections at different points in the reactor this being recorded on an area detector screen. Below is shown a typical diffraction pattern with red and green Debye−Scherrer rings highlighted for the strongest ceria reflections 111 and 113, respectively; this is flanked by two corresponding examples of integration of diffraction intensity around the 111 and 113 rings; diffraction rings coming from steel are deliberately omitted for clarity. The figure also illustrates the geometric broadening (exaggerated in the figure) that results from diffraction contributions by different parts of the mixing zone; for example, ceria 111 and 113 diffractions emanate from positions P_1 and P_2 within the mixing zone.

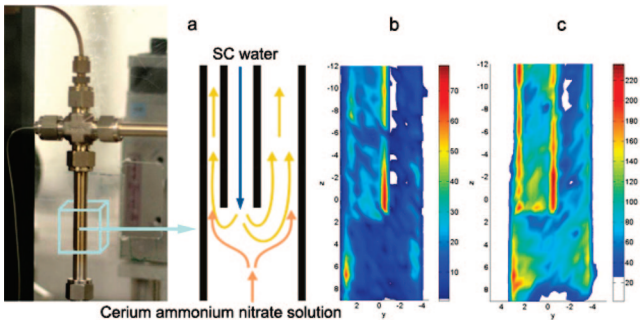

Figure 3. CHFS counter-current mixer and TEDDI results. (a) Photograph and schematic illustration showing the counter-current mixer for continuous production under supercritical water conditions (374 °C, 22.1 MPa) of nanosized CeO_2 particles. The inner and outer stainless steel tubes have diameters of 3.2 and 9.5 mm, respectively. (b) *yz* TEDDI image based on intensities from the ceria 113 reflection observed at 108.5 keV (TEDDI scan = 23 × 29 points, step size = 0.5 × 0.75 mm, collection time = 5 s per point, total scan time 68 min, detector 2θ-angle = 4°). (c) Similar scan to (b) but obtained during the postproduction water-wash cycle. The build up of ceria product on the walls of the inner steel tube and some regions of the outer pipe (inner wall) is clearly evident in (b) and (c).

with supercritical water. The reaction proceeds instantaneously with the formation of phase-pure cubic CeO_2 in the mixing zone.[12,13] To conduct these experiments, it was necessary to fabricate a purpose-built portable CHFS reactor based on a previous laboratory design;[9−13] its chief attributes were a size small enough to fit inside the available synchrotron space and portability to enable quick setup and fast linear scanning during data acquisition.

The overall setup is shown schematically in Figure 1. The two tomographic imaging modes are contrasted, schematically, in Figure 2. The TEDDI mode (Figure 2a) has been previously described in detail.[21−27] It uses a white (polychromatic) collimated synchrotron X-ray beam incident upon the subject of study, from which the diffracted beam is selected at a fixed 2θ angle by means of collimator slits. The collimation system effectively defines a discrete diffracting volume positioned within the subject of study (as depicted in Figure 2a); the resulting diffraction pattern, dispersed in energy, is collected by a solid-state energy-dispersive detector. To construct a tomographic image, it is necessary to scan the subject of study across this diffracting volume, in one-, two-, or three dimensions, using an *xyz* stage so that all regions of interest are visited. Tomographic maps are then subsequently constructed from the dimensional variations of any selected feature in the diffraction patterns, such as the intensity of the 113 ceria peak yielding maps of ceria concentration.

A variation of this principle is termed TADDI, in which the more common diffraction mode, that of monochromatic angle-dispersive diffraction, is used. This is illustrated in Figure 2b in which the powder diffraction pattern appears as uniform Debye−Scherrer rings on a 2D-CCD detector. These powder rings can be integrated to produce the one-dimensional equivalents (i.e., intensity versus 2θ angle) and, from these diffraction patterns, tomographic maps are constructed in analogous fashion to the TEDDI method.

The TEDDI and TADDI modes are found to be complementary in nature. Because of its well-defined collimation system, the TEDDI mode yields higher spatial resolution images. By contrast, TADDI has to collect diffraction rings over a considerable angular range and so the consequent lack of diffracted beam confinement means that its spatial resolution is low along the beam direction (as depicted in Figure 2); however, because the whole diffraction rings are recorded with TADDI, the technique is more sensitive to low sample concentrations.

For the studies reported here, the TEDDI/TADDI data collections were arranged as 2D sections in the *xy*, *yz*, or *zx* planes; the most directly useful are the *yz* sections, which present a "side-view" of the counter-current mixing zone within the vertical stainless steel outer-tube. To compare modes, the same mixing tube configuration was used for both the TEDDI and TADDI imaging; that is, with the steel inner-tube of the counter-current mixing zone (delivering the downward-flowing supercritical water) being asymmetrically offset from the center of the outer-tube (which delivers the upward-flowing cerium ammonium nitrate solution). The detailed experimental specifications (scan details, technical

(21) Harding, G.; Newton, M.; Kosanetzky, J. *Phys. Med. Biol.* **1990**, *35*, 33.
(22) Hall, C.; Barnes, P.; Cockcroft, J. K.; Colston, S. L.; Hausermann, D.; Jacques, S. D. M.; Jupe, A. C.; Kunz, M. *Nucl. Instrum. Methods Phys. Res., Sect. B* **1998**, *140*, 253.
(23) Barnes, P.; Jupe, A. C.; Jacques, S. D. M.; Colston, S. L.; Cockcroft, J. K.; Hooper, D.; Betson, M.; Hall, C.; Barè, S.; Rennie, A. R.; Shannahan, J.; Carter, M. A.; Hoff, W. D.; Wilson, M. A.; Phillipson, M. C. *Nondestr. Test. Eval.* **2001**, *17*, 143.
(24) Jacques, S. D. M.; Pile, K.; Barnes, P.; Lai, X.; Roberts, K. J.; Williams, R. A. *Cryst. Growth Des.* **2005**, *5*, 395.
(25) Tunna, L.; Barclay, P.; Cernik, R. J.; Khor, K. H.; O'Neill, W.; Seller, P. *Meas. Sci. Technol.* **2006**, *17*, 1767.
(26) Beale, A. M.; Jacques, S. D. M.; Bergwerff, J. A.; Barnes, P. B.; Weckhuysen, M. *Angew. Chem., Int. Ed.* **2007**, *46*, 8832.
(27) Cernik, R. J.; Khor, K. H.; Hansson, C.; Roy, J. *J. R. Soc. Interface* **2008**, *5*, 477.

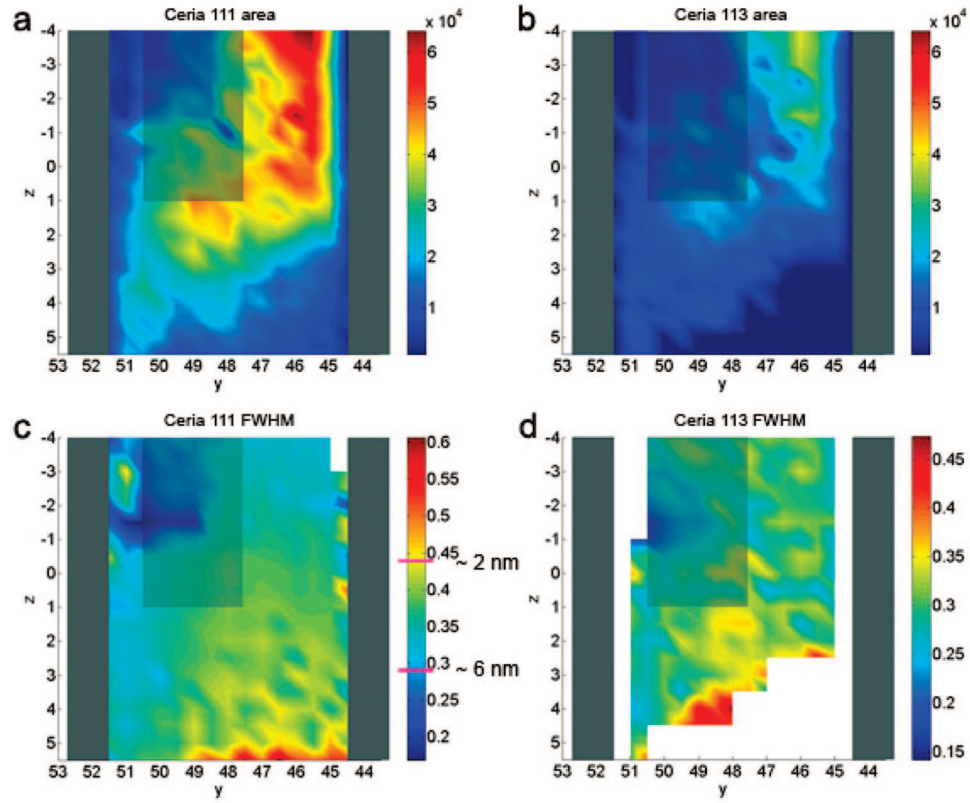

Figure 4. TADDI results obtained from the CHFS counter-current mixer (the tube borders and the internal tube have been added to the images for guidance). (a, b) *yz* TADDI images constructed from the intensity of the strongest ceria reflections, 111 and 113 appearing at $2\theta = 5.14$ and 9.75°, respectively; in both cases, the highest concentration of ceria is found to be above the terminus of the inner-tube and within the wider passage between the walls in the asymmetric tube arrangement. (c, d) *yz* TADDI images constructed from the peak widths of the ceria 111 and 113 reflections; in both cases, the smallest peak widths, which equates to largest average crystallite size, are found to be in the same region of highest intensity in (ab); two representative crystallite sizes are indicated. (TADDI scan = 20 × 20 points, step size = 0.5 × 0.5 mm, collection time = 8 s per point, total scan time = 2 h 11 min; the white area blanks out the regions for which the peaks are almost no longer discernible above the background. For processing these tomograms nearest-neighbor interpolation of pixels was applied.)

values) can be found in the figure captions and the Supporting Information section.

Images b and c in Figure 3 present *yz* TEDDI maps of part of the counter-current mixing zone during and after production of nano-CeO_2 particles constructed from the intensity of the ceria 113 reflection. Figure 3b, taken during operation of the reactor, shows the build-up of a small coating of the ceria product on the walls of the inner steel tube and some regions of the outer pipe (inner wall). This build-up is a result of the long synthesis run times used and was later confirmed when the apparatus was opened up after the experiment. Figure 3c is a subsequent ceria-113 tomogram of the same region later during the washing procedure following a 12 h production cycle. In practice, the reactor pipes and fittings have to be periodically taken apart in order to remove such build-up of deposits of ceria on the inside face of the outer tube and the outer walls of the inner tube. Apart from revealing the build-up of this coating, the CeO_2-based image effectively maps out the true position of the "hidden" inner tube, clearly showing its asymmetric position within the outer tube in this particular experiment.

The images obtained in the TADDI mode are presented in Figure 4; they are based on the strongest ceria reflections, 111 and 113. With TADDI the lack of resolution in the incident beam direction (*x*-axis in the schematic of Figure 2b) effectively renders the CeO_2 tomographic images as *yz* maps of polycrystalline CeO_2 content contained along the beam path inside the tube. This means the image effectively combines, for example, the CeO_2 crystallizing in front of and behind the inner-tube but maintaining meaningful resolution in *yz*. This feature, coupled with the procedure of collecting and integrating diffracted intensities around the whole Debye−Scherrer rings, means that the TADDI images are very sensitive to the CeO_2 forming within the solution rather than localized deposits as with TEDDI (see above). This is as an essential feature of the method as it is difficult to envisage any other current technology being able to image continuous solution nanoparticle products at such low concentrations (ca. 4 wt%). The resulting TADDI images (images a and b in Figure 4) clearly show the overall crystallization zone within the reactor, extending below the terminus of the inner tube and up the inside of the outer tube. One can speculate that in this case, as the inner tube was asymmetrically positioned, it offered an opportunity for crystallization/flow to favor the wider passage between the two tube walls.

Images c and d in Figure 4 show complementary tomographic plots constructed from the peak widths (rather than intensity) of the ceria diffraction rings. The Scherrer equation defines a (inverse) relationship between peak width and

crystallite size, so these images are effectively crystallite size tomographic maps. (The methods section shows the derivation of crystallite sizes from peak widths, the values obtained being more indicative for judging trends than for quoting exact crystallite sizes.) They show broader peaks representing a smaller mean crystallite size of ~2 nm in the flow path just below the terminus of the inner tube where the Ce salt stream first comes into contact with the supercritical water. This suggests that this lower region is one primarily of crystallite nucleation. However, the sharper peaks represent a larger mean crystallite size of ~6 nm, and this occurs in a region around 2−3 mm up from the inner tube terminus within the wider passage between the tube walls. One can therefore conclude that the nanoparticle crystallite growth proceeds in the intervening region and is effectively completed by the top of the scan in Figure 4a, beyond which the process is agglomeration and then transport of crystallized material out of the reactor.

Experimental Section

A custom-made portable CHFS system (Figure 1), based on a previously described [9−13] design, was specifically built for this experiment. The portable frame was made of lightweight aluminum with Perspex walls in order to fit onto the *xyz* stage. It housed the safety pressure release valves, stainless steel tubing pressure gauges, mixing point, cooler and back pressure regulator, and associated Swagelok fittings. The HPLC pumps were connected to the heater and mixing point via flexible high-pressure 1/16″ (1.6 mm) stainless steel tubing with the HPLC pumps themselves not located on the moveable *xyz* stage, but sitting alongside it on a fixed platform. HPLC Pump P1 was used to pump water to the preheater (maintained at 450 °C), whereas pump P2 was used to pump the solution, both at a 25 mL min^{-1} flow rate. The mixture was brought into contact with a superheated water feed in the counter-current mixer, whereupon the hydrothermal reaction took place in a continuous fashion. The slurry from the CHFS system was collected at the exit of the back pressure regulator at ambient pressure.

The experiment was carried out at the high-energy beamline ID15A of the European Synchrotron Radiation Facility (ESRF) in Grenoble, France. Two modes of measurement were employed: TEDDI and spatial scanning ADD. An experimental arrangement was chosen that allowed for fast switching between the two modes (see panels b and c in Figure 1). The same CHFS synthesis setup was used for both modes. In each mode, fine movements of the CHFS reactor about the beam were effected by movements of the *xyz* stage. Two incident beams, monochromatic and white, were spaced at some (50 mm) distance apart and controlled with independent fast shutters. In energy-dispersive mode, an incident white beam of 30−300 keV was used, and the diffraction patterns were collected over the range 80−120 keV by a fixed point single-element EDD detector. The EDD detector and collimator (the latter consisting of two sets of horizontal and vertical slits 0.7 m apart with a brass antiscatter pipe between) were positioned in line-of-sight of the CHFS reactor. In angle-dispersive mode the incident monochromatic beam was set at a wavelength of 0.138 Å (89 keV) and the diffraction patterns were monitored using a MAR-CCD-133 area detector (diameter = 133 mm, pixel size = 64.7 × 64.7 mm^2, set at a sample−detector distance of 370 mm).

Transmission electron microscopy (TEM) and X-ray diffraction (XRD) were used to estimate the crystallite size of the ceria product. A specimen from the slurry collected during the actual ESRF experimental run showed the typical XRD pattern of the cubic phase ceria.

The well-known Scherrer equation gives a simple inverse relationship between peak width and crystallite size (neglecting strain): $L_{hkl} = K\lambda/(\beta_{hkl}\cos\theta)$, where L_{hkl} is the mean crystallite size, β_{hkl} the peak full width at half the maximum intensity at a Bragg angle 2θ, λ the X-ray wavelength, and K a constant approximately equal to unity (0.9). The measured 111 peak width, β_{tot}, is assumed to be related ($\beta_{tot}^2 = \beta_{111}^2 + \beta_{ins}^2$) to the true crystallite peak width, β_{111}, and an instrumental contribution, β_{ins}, which is obtained from a powder pattern of an yttria standard. This yields a mean crystallite size $L_{111} = 6.2 \pm 0.6$ nm.

The TEM analysis showed that the crystallites were typically uniform in size with a mean diameter value of 5.3 nm and a standard deviation 0.7 nm. This TEM value is slightly lower than the XRD value, but they agree within the error limits.

The approach taken in estimating the range of crystallite size in Figure 4 is to relate the measured crystallite size of the outflow material to the smallest peak widths obtained. In this way, the method effectively uses this relationship as a way of calibrating the hitherto unknown instrumental component and then using it for the small particle size regime lower down in Figure 4c.

The working "measured" particle size was taken as the mean of the XRD and TEM evaluations, i.e., $L_{TEM/XRD} = 5.8$ nm. The peak widths in the upper part of the Figure 4c map, $\beta_{map\text{-}outflow}$, are assumed to result from a combination of the actual particle size, $\beta_{TEM/XRD}$, and the TADDI instrument broadening, $\beta_{instrument}$

$$\beta^2_{map\text{-}outflow} = \beta^2_{TEM/XRD} + \beta^2_{instrument} \quad (1)$$

where $\beta_{TEM/XRD} = K\lambda/(L_{TEM/XRD}\cos\theta)$. We can then use $\beta_{instrument}$ to determine the material contribution to the 111 peak width from any other region in the reactor vessel (assuming changes in instrumental contribution are negligible)

$$\beta^2_{111} = \beta^2_{111total} - \beta^2_{instrument} \quad (2)$$

where $\beta_{111total}$ is the uncorrected width. Using the corrected width, β_{111}, in the Scherrer equation gives a crystallite size estimate of $L_{111} \approx 2.0$ nm for the flow path below the inner tube terminus.

Conclusion

In conclusion, we note that the combination of TEDDI and TADDI tomographic techniques (now termed TÆDDI) are capable of revealing the nature of synthesis processes occurring within inhospitable environments such as continuous crystallization of nanoceramics in supercritical water. The two modes are complementary, combining information about localized product build-up and reactor geometry with images of the nanosized crystalline product and crystallite growth, even at low solution phase concentrations. This capability can be considered to be truly investigative; it has revealed the nature of crystallization inside the mixing zone, even distinguishing the nucleation and growth sectors, which extends upward and distinctly to one side of the outer tube as a result of the asymmetric configuration used. In this current form, TÆDDI operates in a slow "point-by-point" mode such that total image collection times are long (typically 1−2 h) and suitable only for imaging static "steady-state" systems such as described here. However, the next generation of detector/collimator arrays will be significantly faster and enable TÆDDI imaging of both transient

and steady state phenomena; this capability will offer great promise for uncovering the true nature of a wide range of processes, including other synthesis systems and industrial applications.

Acknowledgment. We thank EPSRC for research funding ("Synthesis, Design and Function in New Materials Chemistry", ref. EP/D504872/1; "From Laboratory to Pilot Plant", ref. EP/E040551/1), the ESRF and SRS for synchrotron beamtime, Mr. Paul Stukas for building the CHFS reactor frame, and Mr. Martin Vickers for the laboratory diffraction. Johnson Matthey is thanked for supporting the industrial case award (P.B.).

Note Added after ASAP Publication. There was an error in the caption of Figure 4 in the version of this paper published ASAP May 11, 2009; the corrected version published ASAP June 2, 2009.

Supporting Information Available: Continuous hydrothermal flow synthesis (CHFS) system, combined TEDDI and TADDI measurements and TEM analyses of CeO_2 nanoparticles (PDF). This material is available free of charge via the Internet at http://pubs.acs.org.

CM900118Z